



# Ni-Mo nanoparticles as co-catalyst for drastically enhanced photocatalytic hydrogen production activity over g-C<sub>3</sub>N<sub>4</sub>



Xin Han<sup>a</sup>, Dongyu Xu<sup>a</sup>, Lin An<sup>a</sup>, Chengyi Hou<sup>a</sup>, Yaogang Li<sup>b</sup>, Qinghong Zhang<sup>a,b,\*</sup>,  
Hongzhi Wang<sup>a,\*\*</sup>

<sup>a</sup> State Key Laboratory for Modification of Chemical Fibers and Polymer Materials, College of Materials Science and Engineering, Donghua University, Shanghai, 201620, China

<sup>b</sup> Engineering Research Center of Advanced Glasses Manufacturing Technology, MOE, Donghua University, Shanghai, 201620, China

## ARTICLE INFO

### Keywords:

g-C<sub>3</sub>N<sub>4</sub>  
Ni-Mo alloys  
Co-catalyst  
Photocatalyst  
Hydrogen evolution

## ABSTRACT

Photocatalytic water splitting is an environmentally friendly technique for sustainable solar hydrogen production, which requires low-cost and earth-abundant co-catalysts to replace expensive noble metal such as platinum. Herein, for the first time, we demonstrate noble-metal-free Ni-Mo alloys which has been widely attended in the field of electrocatalysis as co-catalysts to drastically enhance the activity of g-C<sub>3</sub>N<sub>4</sub> visible light photocatalyst for H<sub>2</sub> production from water. The novel Ni-Mo/g-C<sub>3</sub>N<sub>4</sub> photocatalyst is in-situ synthesized by an effective and simple one-pot synthesis method. For the synthesized Ni<sub>0.4</sub>Mo<sub>0.6</sub> and with optimized content of 10 wt%, composite photocatalyst Ni<sub>0.4</sub>Mo<sub>0.6</sub>/g-C<sub>3</sub>N<sub>4</sub> shows the champion photocatalytic H<sub>2</sub> generation rate 1785 μmol g<sup>-1</sup> h<sup>-1</sup>, which is about 37 times higher than that of pure g-C<sub>3</sub>N<sub>4</sub>, and comparable to that of the optimized Pt/g-C<sub>3</sub>N<sub>4</sub>. Based on the detailed analyses of UV-vis diffuse reflectance spectroscopy, photoluminescence spectra, photocurrent response curves and electrochemical impedance spectroscopy Nyquist plots, the present good efficiency of Ni-Mo/g-C<sub>3</sub>N<sub>4</sub> is mainly attributed to the presence of Ni-Mo alloys, which effectively promote the separation and suppress the recombination of photogenerated electrons and holes.

## 1. Introduction

Hydrogen (H<sub>2</sub>) as a renewable energy storage is an ideal energy source for mankind, because its combustion can release a lot of energy without the emission of greenhouse gas. Therefore, H<sub>2</sub> production through solar light-driven splitting of water using semiconductor photocatalysts convert solar energy into chemical energy has attracted great scientific interest [1–3]. To date, great efforts have been made for this area by using hundreds of semiconductor photocatalysts. However, the large-scale application of semiconductor photocatalysts was significantly retarded by its sluggish charge transfer, fast electron-hole charge recombination and inefficient surface reaction [4]. Therefore, loading noble-metals (such as Au, Pt and Ru) as extra co-catalysts must be operated to overcome these obstacles and dramatically enhance the photocatalytic activity of photocatalysts. The noble metal co-catalyst with low overpotential and fast kinetics for H<sub>2</sub> generation reaction can significantly promote the separation of photogenerated charges (electrons) from the semiconductor to co-catalysts, which also served as the

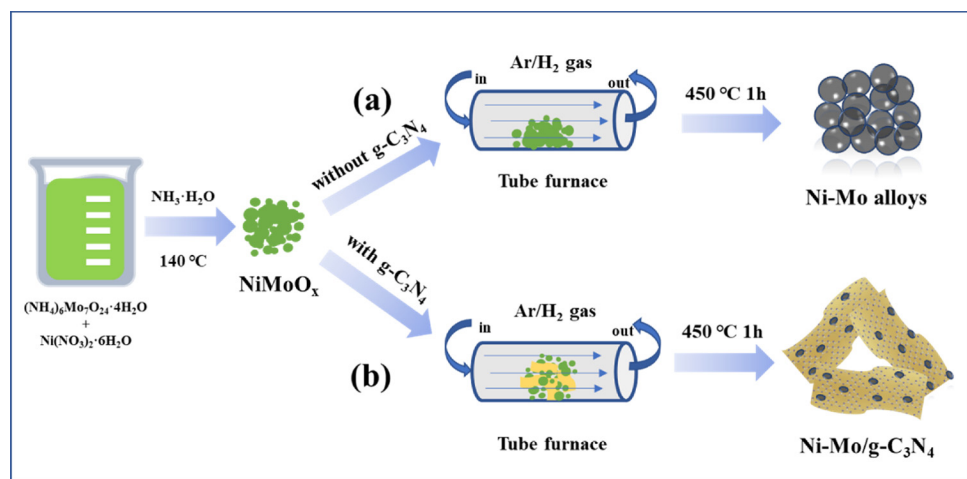
active sites for H<sub>2</sub> evolution [1,2,5]. Unfortunately, the high costs and scarcity of noble-metals make their practical application limitation in the photocatalytic area. Therefore, it is significantly important to explore substitutable low-cost and abundant elements on earth as the co-catalysts [6,7].

In recent years, as a typical metal-free semiconductor photocatalyst for H<sub>2</sub> generation, g-C<sub>3</sub>N<sub>4</sub> composed of the most abundant elements (C and N) on earth has been gotten extreme attention because it is low cost, high chemical and thermal stability, nontoxic nature and has excellent optical properties, since the discovery of g-C<sub>3</sub>N<sub>4</sub> as photocatalysts in 2009 [5,8–13]. However, the single-component g-C<sub>3</sub>N<sub>4</sub> usually exhibits the low photocatalytic H<sub>2</sub> production due to the fast recombination rate of photogenerated charge carriers [14,15]. Therefore, many g-C<sub>3</sub>N<sub>4</sub>-based photocatalysts loaded with noble-metal-free components as effective co-catalysts to inhibit its fast recombination of photogenerated charges have been reported, and the presence of these co-catalysts observably increased the H<sub>2</sub> production activity. Hou et al. significantly improved the H<sub>2</sub> production performance of g-C<sub>3</sub>N<sub>4</sub> under

\* Corresponding author at: State Key Laboratory for Modification of Chemical Fibers and Polymer Materials, College of Materials Science and Engineering, Donghua University, Shanghai, 201620, China.

\*\* Corresponding author.

E-mail addresses: [zhangqh@dhu.edu.cn](mailto:zhangqh@dhu.edu.cn) (Q. Zhang), [wanghz@dhu.edu.cn](mailto:wanghz@dhu.edu.cn) (H. Wang).



**Scheme 1.** The fabrication process of the Ni-Mo alloys (a) and Ni-Mo/g-C<sub>3</sub>N<sub>4</sub> composites (b).

visible light by using WS<sub>2</sub> as co-catalyst to substitute for noble metals [16]. Gu et al. prepared the NiO modified g-C<sub>3</sub>N<sub>4</sub> photocatalysts showed obviously enhanced visible-light photocatalytic H<sub>2</sub> evolution reaction (HER) activity [9]. Zhu et al. reported a binary nanohybrid of two-dimensional black phosphorus (as co-catalyst) and g-C<sub>3</sub>N<sub>4</sub> with significantly improved HER activity under visible and near infrared spectrum region [5]. What's more, Xie et al. were inspired by the excellent performance of NiCoP in the electrocatalysis field and achieved good results by using NiCoP as a co-catalyst of g-C<sub>3</sub>N<sub>4</sub> for photocatalytic H<sub>2</sub> production. Inspired by the above reported work, we note that the noble-metal-free Ni-Mo alloys received a lot of attention as electrocatalysts for H<sub>2</sub> production in electrochemical catalytic field and shows a better electrical performance similar to that of Pt with good electronic conductivity and low overpotential [2,17–21]. Therefore, we believe the Ni-Mo alloys may be used as co-catalyst in photocatalytic field for significantly enhancing photocatalytic H<sub>2</sub> production activity of g-C<sub>3</sub>N<sub>4</sub> by splitting water. However, there is few report up to date.

Herein, Ni-Mo alloys was studied as a non-noble-metal and active co-catalyst for photocatalytic H<sub>2</sub> generation, and the Ni-Mo/g-C<sub>3</sub>N<sub>4</sub> composites were in-situ synthesized by an effective and simple one-pot synthesis method. The photocatalytic H<sub>2</sub> generation activity of the Ni-Mo/g-C<sub>3</sub>N<sub>4</sub> composites was measured under simulated sunlight and visible light irradiation. The results shown that the activity of the Ni-Mo/g-C<sub>3</sub>N<sub>4</sub> photocatalysts for H<sub>2</sub> generation was obviously enhanced as compared to that of g-C<sub>3</sub>N<sub>4</sub>. It is mentionable that the non-noble-metal Ni-Mo alloys co-catalyst has comparable activity to Pt for photocatalytic H<sub>2</sub> generation. Finally, the possible photocatalytic mechanism of the Ni-Mo/g-C<sub>3</sub>N<sub>4</sub> composites was proposed and discussed in detail.

## 2. Experimental section

### 2.1. Preparation of g-C<sub>3</sub>N<sub>4</sub> nanosheets

The g-C<sub>3</sub>N<sub>4</sub> nanosheets were prepared by a facile calcination process reported previously [22]. The typical process is as follows: 10.0 g of melamine powders were put into a suitable alumina crucible with a cover and calcined at 600 °C for 5 h at a rate of 5 °C/min. The resulted yellow products were ground by a mortar and screened by a 200-mesh sieve. Then the resulted yellow bulk g-C<sub>3</sub>N<sub>4</sub> was uniformly placed in an alumina boat with enough size, and heated to 520 °C for 6 h at a heating rate of 2 °C/min. After this calcination process, the yellow bulk g-C<sub>3</sub>N<sub>4</sub> become into white g-C<sub>3</sub>N<sub>4</sub> nanosheets and abbreviated as g-CN.

### 2.2. Preparation of Ni-Mo nanopowders and Ni-Mo/g-C<sub>3</sub>N<sub>4</sub> composites

A sample synthetic procedure for Ni-Mo nanopowders with a 6/4

atomic ratio of Ni/Mo is described below according a previously report [17]. 0.6 g ammonium heptamolybdate and 1.5 g nickel nitrate hexahydrate were mixed using 5 mL deionized water, and then the solution was added into 2.0 mL ammonium hydroxide (28%). After the molybdate salt dissolved, 45 mL diethylene glycol was added to the solution at room temperature. Then the mixture was heated on a thermostatic oil-bath set to 200 °C with vigorously stirring. When the water in the mixture began to boil (almost 140 °C), the reaction was removed from the oil-bath, and cooled for 30 s in air. While still hot, the suspension was centrifuged at 8000 rpm for 6 min, and washed with water for 5 times. After a subsequent washing with acetone, the precipitate was dried at 60 °C, yielding a pale green solid, and marked as NiMoO<sub>x</sub>. Afterwards, the above green solid was heated in a tube furnace under flowing Ar/H<sub>2</sub> gas mixture (5% H<sub>2</sub>), first at 200 °C for 30 min, and then at 450 °C for 1 h with a heating rate of 5 °C/min. After cooled down, the Ni-Mo nanopowders with a 6/4 ratio of Ni/Mo were successfully prepared. The other varying atomic ratio of Ni and Mo were prepared by adjusting the ratio of ammonium heptamolybdate and nickel nitrate hexahydrate.

Ni-Mo/g-C<sub>3</sub>N<sub>4</sub> composites were prepared by following method. The synthesized g-CN (0.1 g), and varying amounts of the synthesized NiMoO<sub>x</sub> were dispersed in a mortar, which was then added an appropriate amount of ethanol and thoroughly ground. The subsequent reduction process was the same as for the preparation of Ni-Mo nanopowders. The fabrication process of the Ni-Mo alloys and Ni-Mo/g-C<sub>3</sub>N<sub>4</sub> composites was shown in Scheme 1. The weight ratios of NiMoO<sub>x</sub> to the g-CN were 5 wt%, 10 wt% and 20 wt%, respectively. The obtained samples were labelled as Ni<sub>x</sub>Mo<sub>y</sub>/CN-z, where x and y represent the molar ratio of Ni and Mo in Ni-Mo nanopowders, respectively, while z represent the weight ratios of parent NiMoO<sub>x</sub> to the g-CN (z = 5, 10 or 20), such as Ni<sub>0.4</sub>Mo<sub>0.6</sub>/CN-5 and Ni<sub>0.5</sub>Mo<sub>0.5</sub>/CN-10. What's more, to simplify the description of Ni<sub>0.4</sub>Mo<sub>0.6</sub> and Ni<sub>0.4</sub>Mo<sub>0.6</sub>/CN-10 further abbreviated as NiMo and NiMo/CN, respectively. The Ni/CN-10 sample was prepared in the same way, but in absence of ammonium heptamolybdate. Moreover, in order to rule out the impact of H<sub>2</sub> treatment on the g-CN, the control experiment was performed under identical synthesis conditions without adding NiMoO<sub>x</sub> into the reactants, and the as-obtained sample is named as g-CN-H.

### 2.3. Characterization of the photocatalysts

The crystalline phase of all samples was characterized by powder X-ray diffraction (XRD) with a model D/Max-2550 (Rigaku Co., Japan) diffractometer using Cu Ka irradiation ( $\lambda = 1.5406 \text{ \AA}$ ) in 5–90° 2θ range. Transmission electron microscopy (TEM) and high-resolution TEM (HRTEM) images and element mapping were taken using a JEM-

2100 F TEM (JEOL Tokyo, Japan) at an accelerating voltage of 200 kV. UV-vis diffuse reflectance spectra (UV-vis DRS) data were collected using a Perkin-Elmer Lambda 950 spectrophotometer (USA) at room environment. Valence band (VB) X-ray photoelectron spectroscopy (XPS) and XPS spectra were determined on a photoelectron spectrometer (Escalab 250Xi, Thermo Scientific, USA). Nitrogen adsorption-desorption isotherms were performed at 77 K using an Autosorb-1-MP (Quantachrome, USA) automated surface and pore size analyzer instrument. The photoluminescence spectra (PL) and transient fluorescence spectra of samples were measured on a PTI QM/TM/NIR system (Photon Technology International, USA) at room temperature. The contents of Ni and Mo in each sample were analyzed using an inductively coupled plasma-optical emission spectrometer (ICP-OES, Prodigy ICP, USA).

Photoelectrochemical and electrochemical were measured by a VSP-300 (Bio-Logic, France) multichannel potentiostat with a three-electrode cell using g-CN and NiMo/CN films on FTO as the working electrodes, Ag/AgCl electrode as the reference electrode and Pt plate as the counter electrode in 0.5 M  $\text{Na}_2\text{SO}_4$  solution. A 300 W Xe lamp (Perfectlight Co., Beijing, China) was applied as the simulated solar light source (light intensity was determined to be 0.37 W/cm<sup>2</sup> by using a Model 91,150 V Newport Oriel PV reference cell system). The photocurrent measurement was taken at an applied potential of 0 V vs Ag/AgCl. The electrochemical impedance spectroscopy (EIS) was carried out in the frequency range from  $10^{-2}$  to  $10^6$  Hz.

#### 2.4. Photocatalytic $\text{H}_2$ production performance

The  $\text{H}_2$  generation experiments were performed in a closed gas evacuation and circulation light catalytic reaction system (Labsolar-III AG, Perfectlight Co., Beijing) equipped with a top-irradiation optical quartz window. In the typical representative photocatalytic  $\text{H}_2$  generation experiment, 20.0 mg of the catalyst was suspended to 100 mL of a 10% (v/v) triethanolamine (TEOA) solution by a magnetic stirrer. The above suspension was evacuated 15 min to remove air from the system prior to irradiation under a 300 W xenon lamp (Perfectlight Co., Beijing, China) and the reactions were accomplished at room temperature by circulating water. The artificial solar light irradiation was provided without using any filters and a  $\lambda \geq 420$  nm cut-off filter was used for visible light irradiation. Throughout the whole  $\text{H}_2$  generation experiments, the gas concentration of the system was balanced by a fan inside the system. The evolved  $\text{H}_2$  gas was collected every hour and quantified by a gas chromatography (GC-7900, Techcomp, China) using thermal conductivity detector (TCD). The apparent quantum efficiency (AQE) value was calculated by the following equation.  $\text{AQE} = \frac{2 \times \text{number of evolved } \text{H}_2 \text{ molecules}}{\text{number of incident photons}} \times 100\%$ .

### 3. Results and discussion

The Ni-Mo co-catalyst was synthesized through reduction of precipitate from an ammonium molybdate  $[(\text{NH}_4)_6\text{Mo}_7\text{O}_{24} \cdot 4\text{H}_2\text{O}]$  and nickel nitrate  $[\text{Ni}(\text{NO}_3)_2 \cdot 6\text{H}_2\text{O}]$  mixture in a tubular oven in  $\text{Ar}/\text{H}_2$  gas at 450 °C. During this process, the  $(\text{NH}_4)_6\text{Mo}_7\text{O}_{24} \cdot 4\text{H}_2\text{O}$  and  $\text{Ni}(\text{NO}_3)_2 \cdot 6\text{H}_2\text{O}$  derived precipitate was reduced to Ni-Mo metal particles by  $\text{H}_2$  [17]. The content of Ni and Mo loaded on the Ni-Mo/g-C<sub>3</sub>N<sub>4</sub> samples was determined by ICP-OES measurement (see Table S1). The ICP-OES results suggest that the estimated Ni/Mo ratio in the sample is in good agreement with the prescribed values.

All samples were evaluated by the XRD and to investigate the crystal structure of the synthesized g-CN, NiMo and Ni-Mo/g-C<sub>3</sub>N<sub>4</sub> samples. As shown in Fig. 1, the XRD pattern of the NiMo sample has three discernible diffraction peaks, which confirms the structure of Ni metal according to the JCPDS No. 04-0850 [23,24]. The diffraction peaks of Mo species could not be detected because Ni and Mo metals formed a substitutional solid solution with Ni as solvent and Mo as solute during

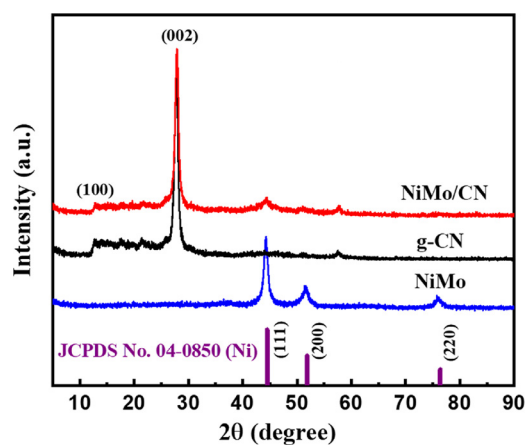


Fig. 1. XRD patterns of the g-CN, NiMo and NiMo/CN samples.

the reduction process, which was consistent with the results reported before [19,20,25,26]. In addition, one can find that the XRD pattern of all the NiMo/CN sample shows the distinct diffraction peaks located at 27.8° (002) and 13.0° (100) corresponding to the stacking and the in-planar packing of the conjugated aromatic system of g-CN [8,9,27,28], and three distinct diffraction peaks at 44.2°, 51.5° and 76.0° for the (111), (200) and (220) plane diffraction assigned to Ni of the Ni-Mo alloy. Fig. S1a shows the XRD patterns of g-CN, NiMo and Ni<sub>x</sub>Mo<sub>y</sub>/CN-10 with different Ni/Mo molar ratio. There is no obvious change in the XRD characteristic diffraction peak of the Ni-Mo/g-C<sub>3</sub>N<sub>4</sub> samples due to Mo complete dissolution in Ni-Mo alloy. In Fig. S1b, it can be seen that with increasing of the Ni-Mo alloys concentration, the intensity of diffraction peaks for Ni-Mo metal increases, while that of the g-CN decreases. In addition, there is no detective diffraction peak of Ni or Mo oxides such as NiO or MoO<sub>3</sub> in the XRD pattern, indicating that the Ni-Mo alloys was complete reduced in flowing Ar-H<sub>2</sub> and not oxidized during cooling and storage. The successful deposition of Ni-Mo alloy nanocrystals on g-CN also can be evidenced by the combined results of elemental mapping and XPS.

Furthermore, HRTEM and TEM are used to characterize the morphology and crystallite size of the as-prepared NiMo/CN sample. Fig. 2a shows that the Ni-Mo nanoparticles distribute randomly on the surface of g-CN. Fig. 2b shows that Ni-Mo nanoparticles have an average diameter of about 5–10 nm, which disperse well onto the surface of g-CN to form a heterojunction. The interface between g-CN and Ni-Mo nanoparticles were also found. The HRTEM image in Fig. 2c shows that the Ni-Mo nanoparticles are uniformly dispersed and are closely attached to form an intimate interface with g-CN, suggesting a good interface between g-CN and Ni-Mo alloys. As shown in Fig. 2d and e, the lattice spacings measured for the crystalline planes are 0.20 nm and 0.18 nm, corresponding to the d values of the (111) and (200) planes for Ni metal, respectively. As shown in the XRD patterns, no lattice of Mo metal was found here. More importantly, the elemental mapping image of C, N, Ni and Mo displayed in Fig. 2f also confirms the existences of Ni and Mo elements. Meanwhile, the elemental mapping also suggests a good dispersion of Ni-Mo nanoparticles on the surface of g-CN.

The interaction of the Ni-Mo alloys with the g-C<sub>3</sub>N<sub>4</sub> support was studied by FT-IR spectroscopy. Fig. S2 shows the typical FT-IR spectra of the g-CN, NiMo and NiMo/CN composite samples. As can be seen, the peak at 810 cm<sup>-1</sup> could be contributed to the characteristic breathing mode of triazine units in g-CN. Additionally, characteristic bands in the 1800–1000 cm<sup>-1</sup> region dominate the spectrum, with peaks appearing at 1637 cm<sup>-1</sup>, 1573 cm<sup>-1</sup>, 1420 cm<sup>-1</sup>, 1324 cm<sup>-1</sup>, and 1250 cm<sup>-1</sup>, could be contributed to the typical stretching modes of CN heterocycles [11,29]. In the case of the NiMo/CN composite, the bands for both g-CN and Ni-Mo alloys appear, corroborating the formation of a composite photocatalysts.  $\text{N}_2$  adsorption-desorption isotherms were measured to

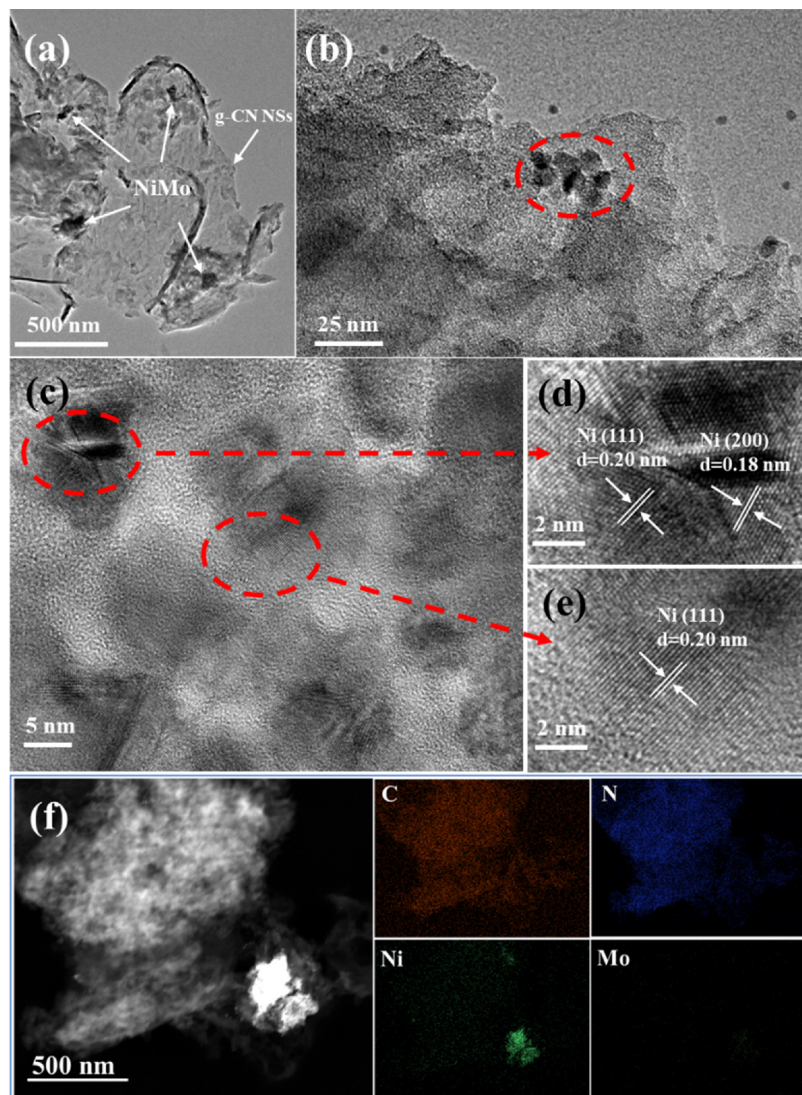


Fig. 2. TEM (a, b), HRTEM (c, d, e) and elemental mapping (f) image for the NiMo/CN sample.

estimate the specific surface area and pore volume of the materials. The Brunauer-Emmett-Teller (BET) specific surface area, pore radius and pore volume obtained for Ni-Mo/g-C<sub>3</sub>N<sub>4</sub> photocatalysts are 81.3 ~ 128.1 m<sup>2</sup>/g, 6.0 ~ 8.6 nm and 0.43 ~ 0.58 cm<sup>3</sup>/g (Fig. S3 and Table S2), respectively. The change of Ni/Mo ratio or Ni-Mo alloys content (5 wt% ~ 20 wt%) in Ni-Mo/g-C<sub>3</sub>N<sub>4</sub> photocatalysts have no obvious effect on the pore volume and BET specific surface area of the photocatalyst, due to a small number of alloys as well as a finer crystallize size of Ni-Mo alloy. Additionally, the smaller specific surface areas of Ni-Mo/g-C<sub>3</sub>N<sub>4</sub> photocatalysts compared with g-CN may be due to the larger specific gravity of Ni-Mo alloys and the strong coupling between Ni-Mo nanoparticles and g-CN reduces repulsive forces [30].

XPS measurements were also carried out to investigate the valence state and surface chemical composition of the NiMo/CN sample. As shown in Fig. 3a, the C 1 s XPS spectrum reveals that the characteristic sp<sup>2</sup> C = N and C-C species of the s-triazine ring and aromatic rings of g-CN are presented at binding energies of 288.1 eV and 284.6 eV, respectively. The N 1 s XPS spectrum (Fig. 3b) proves the existences of C–N = C, N–(C)<sub>3</sub>, C–N–H and  $\pi$  excitations of the C = N conjugated structures from g-CN, which are located at 398.7 eV, 399 eV, 400.9 eV and 404.5 eV, respectively [9,31,32]. The results give evidence of the minimal disturbance of N- and C- containing chemical entities in the composite photocatalysts with respect to the bare g-CN reference (Fig. S4), so Ni-Mo alloys deposition makes little chemical modification of

the g-C<sub>3</sub>N<sub>4</sub> support. Fig. 3c shows the XPS spectra of Ni 2p, and the characteristic peak of 852.1 eV could be find and corresponding with Ni (0) metal (852.6 eV) and other peaks were attributed to the satellite peak [4,33]. In addition, the typical XPS spectra of Mo 3d (Fig. 3d) can be decomposed into two peaks with 231.8 eV and 228.9 eV correspond to Mo (0) metal (231.2 eV and 228.4 eV) [34]. We can find that the Ni metal and Mo metal XPS peak of the NiMo/CN sample was slightly shifted to a lower or a higher value about 0.5 eV compared to their corresponding binding energy peak, respectively. The shift of the binding energy is due to the slight electron transfer from Mo to Ni, which may lead to an enhanced photocatalytic activity for H<sub>2</sub> production [35]. According to the XPS results, both Ni and Mo metal existed on the surface of Ni-Mo/g-C<sub>3</sub>N<sub>4</sub> composites can be further confirmed.

To identify the optical properties effect of the g-CN after Ni-Mo alloys modification, the light-absorption properties of g-CN and a series of Ni-Mo/g-C<sub>3</sub>N<sub>4</sub> photocatalysts were measured by UV-vis DRS spectroscopy. Fig. 4a and b shows the UV-vis DRS spectra of g-CN, Ni<sub>x</sub>Mo<sub>y</sub>/CN-10 with different Ni/Mo ratio and Ni<sub>0.4</sub>Mo<sub>0.6</sub>/CN with various concentrations of Ni-Mo alloys, respectively. The UV-vis DRS results show that the Ni-Mo/g-C<sub>3</sub>N<sub>4</sub> sample has a significantly higher absorption intensity of light than bare g-C<sub>3</sub>N<sub>4</sub> sample, which is mainly caused by the mixing of metallic Ni-Mo alloys and g-CN. The further enhanced light absorbance at wavelength beyond 450 nm is due to the stronger absorption of coefficient by the metal. In addition, the absorption edge

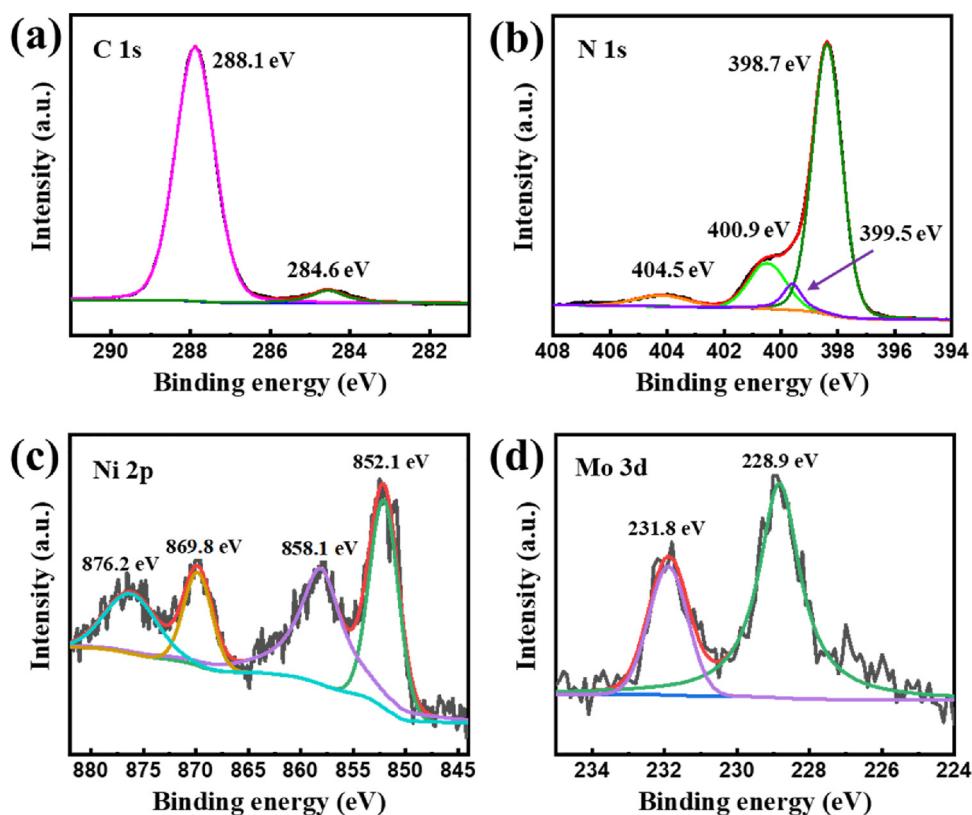


Fig. 3. XPS spectra of (a) C 1s, (b) N 1s, (c) Ni 2p and (d) Mo 3d in the NiMo/CN sample.

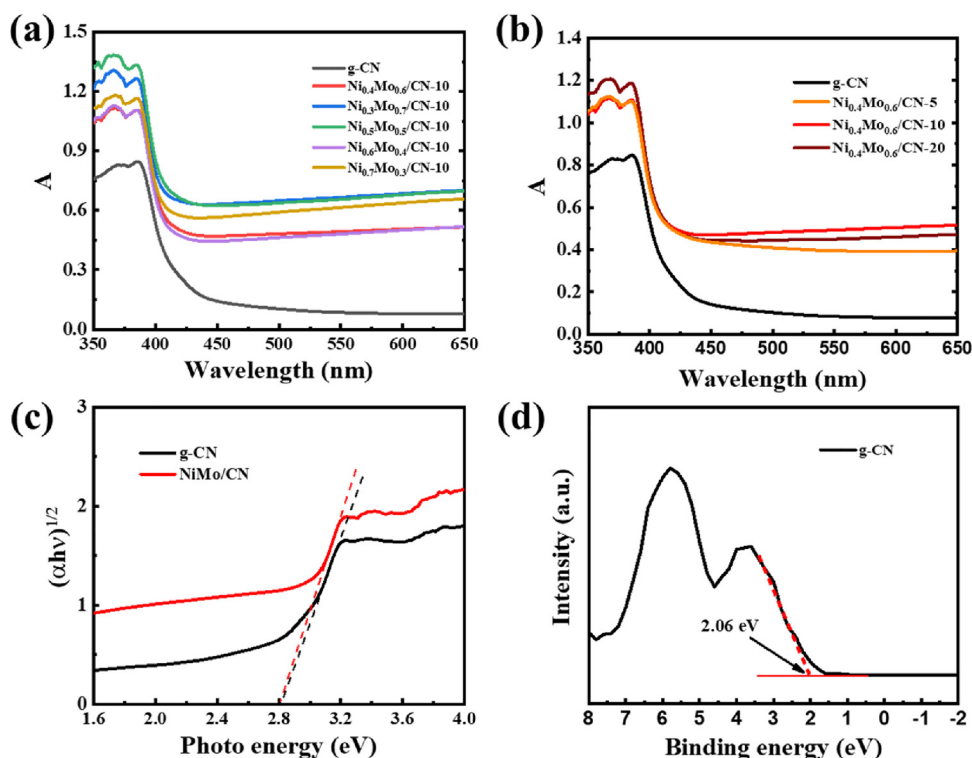
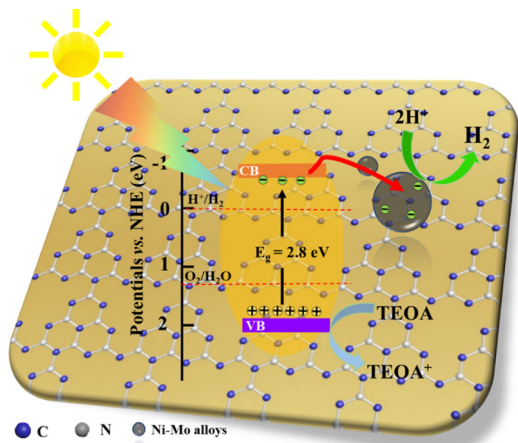


Fig. 4. (a) UV-vis DRS spectra of g-CN and Ni<sub>x</sub>Mo<sub>y</sub>/CN-10 with different Ni/Mo ratio, (b) UV-vis DRS spectra of g-CN and Ni<sub>0.4</sub>Mo<sub>0.6</sub>/CN samples with various concentrations of Ni-Mo alloys, (c) Tauc plot of g-CN and NiMo/CN samples and (d) valence band XPS spectra of g-CN.



**Scheme 2.** The possible mechanism of photocatalytic H<sub>2</sub> evolution reaction on Ni-Mo/g-C<sub>3</sub>N<sub>4</sub> photocatalysts.

and the band-gaps (2.8 eV, Fig. 4c) of g-CN is not shifted after Ni-Mo alloys loading, revealing that Ni-Mo was tightly deposited on the surface of g-C<sub>3</sub>N<sub>4</sub> instead of being doped into the g-C<sub>3</sub>N<sub>4</sub> lattice [36]. Furthermore, the VB state of the g-CN sample was analyzed by VB XPS as shown in Fig. 4d and the band structures of Ni-Mo/g-C<sub>3</sub>N<sub>4</sub> photocatalysts was shown in Scheme 2.

In the typical representative photocatalytic experiment, photocatalytic H<sub>2</sub> generation activity for various samples was tested using TEOA as a hole acceptor. No appreciable H<sub>2</sub> was observed when Ni-Mo alloys alone was used under light irradiation, revealing that Ni-Mo alloys is not an active photocatalyst. Bare g-CN showed photocatalytic activity for H<sub>2</sub> evolution but not with an efficient rate (of 48 μmol g<sup>-1</sup> h<sup>-1</sup>). The reason is that the separation efficiency of its own photogenerated electrons and holes are low exceedingly, leading to the number of electrons that escape from its internal to the surface are few.

Therefore, it makes the probability of electron combined with H<sup>+</sup> decrease in the g-CN surface [33]. Moreover, the photocatalytic H<sub>2</sub> production activity of g-CN-H with Ar/H<sub>2</sub> calcination treatment was also tested and the result showed a similar rate (of 50 μmol g<sup>-1</sup> h<sup>-1</sup>) as that of g-CN without Ar/H<sub>2</sub> calcination treatment, showing that further Ar/H<sub>2</sub> calcination treatment did not fundamentally change the g-CN photocatalytic activity (Fig. S5). Figs. 5a and S6 show the H<sub>2</sub> generation over g-CN and Ni<sub>x</sub>Mo<sub>y</sub>/CN-10 samples with different Ni/Mo ratio under solar light irradiation. It can be clearly seen that the loading of Ni-Mo alloys on the g-CN surface can remarkably improve the H<sub>2</sub> evolution rate of g-CN. One can find that only using Ni nanoparticles decorated on g-CN (Ni/CN-10 sample) also can improve the photocatalytic H<sub>2</sub> production performance of g-CN, but the effecting is not as good as that of Ni-Mo alloys, indicating the photocatalytic H<sub>2</sub> production activity of the Ni-Mo/g-C<sub>3</sub>N<sub>4</sub> photocatalysts is related to the proportion of both Ni and Mo in the sample. When the ratio of Ni/Mo in Ni-Mo alloys is 4:6, the Ni-Mo/g-C<sub>3</sub>N<sub>4</sub> photocatalyst exhibited a highly enhanced H<sub>2</sub> evolution rate as high as of 1785 μmol g<sup>-1</sup> h<sup>-1</sup>, which is about 37 times higher than that of bare g-CN. Besides, in order to research the effect of Ni-Mo alloys content on the photocatalytic H<sub>2</sub> generation performance of g-CN, the photocatalytic activities of the Ni<sub>0.4</sub>Mo<sub>0.6</sub>/CN and Ni<sub>0.6</sub>Mo<sub>0.4</sub>/CN samples with different Ni-Mo alloys amount were measured, and respectively shown in Fig. 5b and c. With the increase of Ni-Mo alloys content from 5 wt % to 20 wt %, both the Ni<sub>0.4</sub>Mo<sub>0.6</sub>/CN and Ni<sub>0.6</sub>Mo<sub>0.4</sub>/CN samples showed the same trend, and when the Ni-Mo content was 10 wt %, the champion photocatalytic hydrogen production performance of the Ni<sub>0.4</sub>Mo<sub>0.6</sub>/CN and Ni<sub>0.6</sub>Mo<sub>0.4</sub>/CN photocatalysts was achieved, and the hydrogen production (3 h) was 5149 and 2184 μmol g<sup>-1</sup>, respectively. The result show that there is an optimum proportion of Ni-Mo alloys addition, and it is about 10 wt %. On the one hand, too little Ni-Mo metal addition is insufficient to provide sufficient photocatalytic reaction sites, and on the other hand, excessive Ni-Mo metal addition could cause a decrease in the effective light harvesting of the photocatalysts.

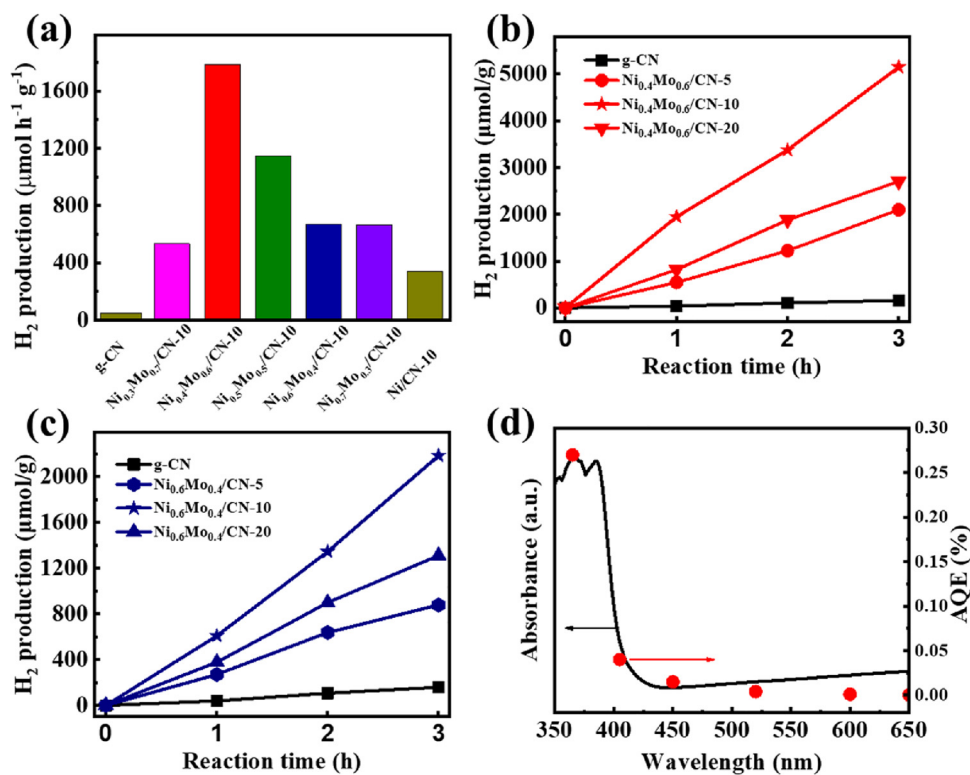


**Fig. 5.** H<sub>2</sub> generation rate of g-CN and Ni<sub>x</sub>Mo<sub>y</sub>/CN-10 with different Ni/Mo ratio (a), photocatalytic H<sub>2</sub> evolution over Ni<sub>0.4</sub>Mo<sub>0.6</sub>/CN (b) and Ni<sub>0.6</sub>Mo<sub>0.4</sub>/CN (c) with different Ni-Mo alloys amount under solar light irradiation, (d) the wavelength-dependent AQE for the NiMo/CN sample.

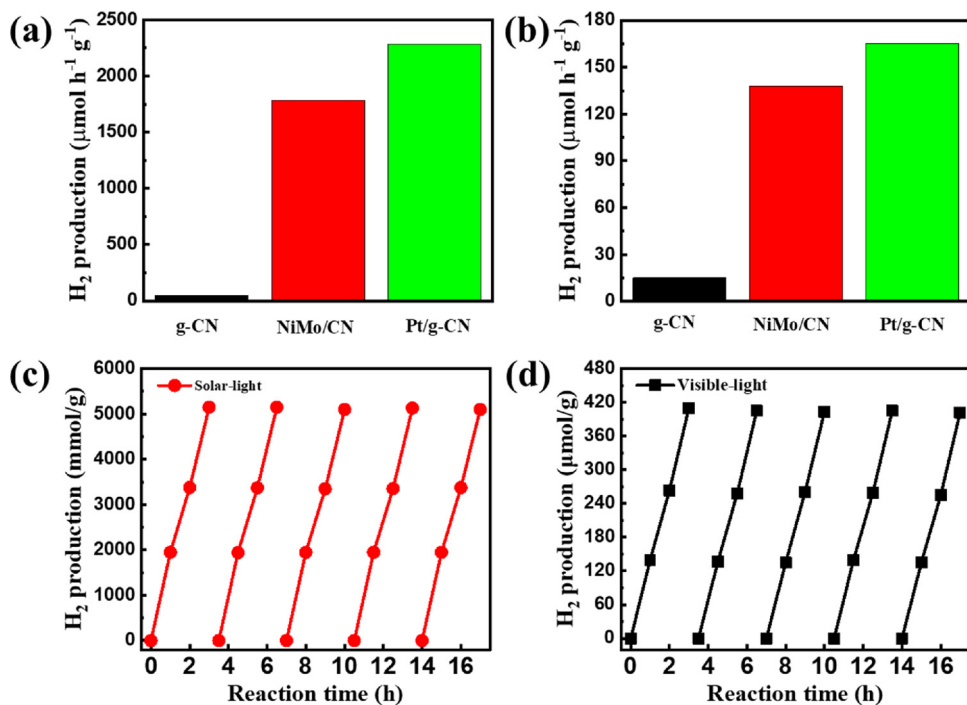


**Fig. 6.** Photocatalytic H<sub>2</sub> evolution over the g-CN, NiMo/CN and Pt/g-CN samples under simulated solar light (a) and visible light (b), and cycling runs for photocatalytic H<sub>2</sub> evolution in the presence of the NiMo/CN sample under simulated solar light (c) and visible light (d) irradiation.

The photocatalytic H<sub>2</sub> production performance of the NiMo/CN photocatalyst was also measured under visible light irradiation and shown in Fig. S7. The results show that the H<sub>2</sub> production activity of the photocatalysts had been significantly enhanced and the hydrogen production after 3 h reached 400 μmol g<sup>-1</sup> which almost 9 times higher than bare g-CN, indicating the photocatalytic activity of H<sub>2</sub> generation ability have got enhanced compared with pure g-CN under the same experimental conditions as the reagent and light irradiation. We have also investigated the photocatalytic H<sub>2</sub> evolution (Fig. S8) and AQE (Fig. 5d) of the NiMo/CN sample at different irradiation wavelength to study more details on the enhanced photocatalytic hydrogen production activity. We can find that AQE at wavelengths less than 520 nm regions approximately corresponded to its optical absorption spectrum. When the wavelength is greater than 520 nm, AQE is almost zero, indicating that the H<sub>2</sub> generation is primarily driven by photogenerated electrons in g-C<sub>3</sub>N<sub>4</sub> [37].

Since Pt is a well-known active co-catalyst for HER and it has been used to enable significant performance for H<sub>2</sub> generation, we also tested the H<sub>2</sub> evolution activities of 2 wt% Pt/g-CN prepared by using the in-situ photo-deposition method for comparison under solar light and visible light irradiation (Fig. 6a and b), and the photo-deposition of Pt on the g-CN resulted in a uniform dispersion of ultrafine Pt nanoparticles (~1–2 nm) [38]. It is interesting to note that the H<sub>2</sub> generation rate of the NiMo/CN photocatalyst is comparable to that of Pt/g-CN, indicating that Ni-Mo alloys is an excellent co-catalyst for promoting highly efficient photocatalytic H<sub>2</sub> production in the present system. It is foreseeable that by more suitable method deposition of the Ni-Mo alloys with uniform dispersion and smaller particles on the surface of the g-CN, like the Pt/g-CN, which can further reduce its amount and improve the performance. These results indicated that it is practical to use the much cheaper Ni-Mo alloys to replace noble Pt as an effective H<sub>2</sub> evolution co-catalyst for g-CN. Further tests were performed to confirm the photocatalytic stability of the NiMo/CN photocatalyst. The reaction system was evacuated every 3 h and the process was carried out for 5 cycles. Fig. 6c and d show the stability of photocatalytic H<sub>2</sub> evolution using the NiMo/CN photocatalyst under solar light and visible light irradiation at room temperature, respectively.

After 5 cycles testing, the H<sub>2</sub> evolution rate of the catalyst showed no significant decrease. Moreover, the structure of NiMo/CN and state of Ni-Mo alloys on NiMo/CN remains unchanged after reaction (Fig. S9). These results indicate that the Ni-Mo/g-C<sub>3</sub>N<sub>4</sub> photocatalysts and the present artificial photosynthetic H<sub>2</sub> generation system are highly efficient and quite robust under light irradiation. In addition, the photocatalytic H<sub>2</sub> generation properties of the NiMo/CN sample increased significantly compared to that of g-CN under different electron donors as sacrificial agents (Fig. S10), indicating that the Ni-Mo nanoparticles can be used as an effective co-catalyst to improve the activity of g-C<sub>3</sub>N<sub>4</sub>.

In order to explore the photocatalytic mechanism of the excellent photocatalytic activity for the Ni-Mo/g-C<sub>3</sub>N<sub>4</sub> photocatalyst, the multiple spectroscopic and photoelectrochemical research were measured. The photoluminescence spectrum was carried out with an excitation wavelength of 365 nm at room atmosphere. Fig. 7a shows the PL intensity of the NiMo/CN and g-CN samples. The obvious PL emission peak for the bare g-CN at 440 nm can be observed, originated from the strong recombination of the photogenerated holes and electrons [39]. As compared to g-CN, the PL emission intensity of the NiMo/CN photocatalyst is dramatically decreased, indicating that the low possibility of carries recombination of the sample. The result suggests the existence of Ni-Mo alloys leads to remarkable suppression of electron-hole recombination in the Ni-Mo/g-C<sub>3</sub>N<sub>4</sub> photocatalyst and can effectively optimize electronic structure of bare g-C<sub>3</sub>N<sub>4</sub> [40,41]. The nanosecond-level time-resolved PL decay spectra of the g-CN and NiMo/CN samples was shown in Fig. 7b. It can be seen that the NiMo/CN sample also showed a distinctly faster decay in the time-resolved PL spectra, indicating the improvement of charge separation from g-CN to the Ni-Mo co-catalysts. Moreover, the calculated average fluorescent lifetime (3.04 ns) of the NiMo/CN sample is shorter than that of bare g-CN (4.74 ns), as shown in Table S3. This result also implies that an additional nonradiative decay channel may be opened through the electron transfer from g-CN to Ni-Mo nanoparticles and effective suppression of the electrons and holes recombination [14,36,42], which is consistent with the PL results. The interaction coupling between Ni-Mo and g-CN could optimize its electronic structure and effectively suppress the recombination of the photogenerated electrons and holes, and thus

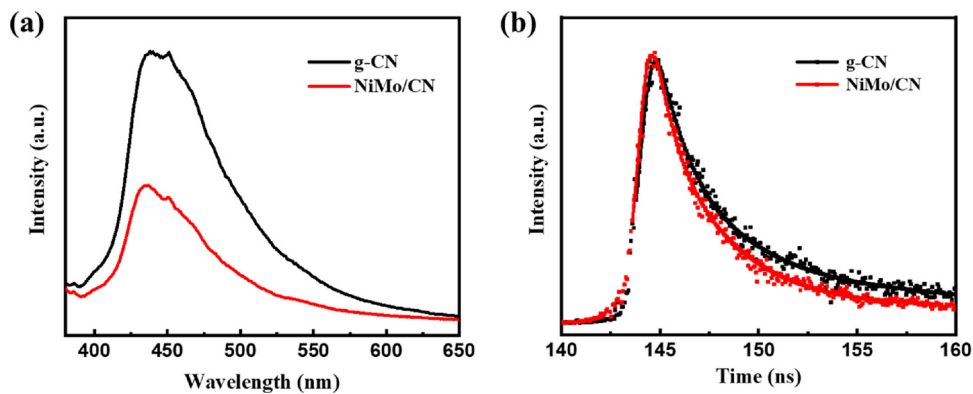


Fig. 7. Fluorescence (a) and nanosecond-level time-resolved fluorescence decay spectra (b) of the g-CN and NiMo/CN samples.

promote the photocatalytic H<sub>2</sub> generation reaction.

To further evaluate the charge-transfer properties of the NiMo/CN sample, transient photocurrent response and EIS were carried out. Fig. 8a shows a sensitive and reproducible transient photocurrent responses of the g-CN and NiMo/CN photocatalysts during on/off irradiation cycles under light. The photocurrent density generated from the NiMo/CN sample is about 8.0 mA cm<sup>-2</sup>, about 25 times higher than that of g-CN, which is consistent with the trend in their photocatalytic H<sub>2</sub> generation activities. The much higher photocurrent density generated for the NiMo/CN sample reflects a better light response and more efficient separation of electrons and holes compared with pure g-CN [43]. Furthermore, the fitted semicircle diameter based on the EIS Nyquist plots shows that the NiMo/CN sample afford smaller charge-transfer resistance (Fig. 8b), further confirming the superior charge separation of photogenerated electrons and holes. The high transfer and separation efficiency of photogenerated electrons and holes is due to the metallic Ni-Mo alloys co-catalyst, which attracts and transfers the photogenerated electrons into the surface of Ni-Mo alloys, and promotes the H<sub>2</sub> production from water [44].

Based on above analyses, the enhanced photocatalytic H<sub>2</sub> production mechanism of the Ni-Mo/g-C<sub>3</sub>N<sub>4</sub> photocatalyst was presented and described in Scheme 2. When the Ni-Mo/g-C<sub>3</sub>N<sub>4</sub> photocatalyst exposed to the light irradiation, the electrons can be excited to the conduction band (CB) from the VB of g-CN, leaving the holes on the VB of g-CN, and generating photogenerated holes and electrons. The photogenerated electrons further quickly transfer to Ni-Mo nanoparticle co-catalysts due to its outstanding metallic property and HER activity. Finally, the electrons aggregate on the surface of Ni-Mo alloys and then reduce H<sub>2</sub>O to release H<sub>2</sub>. Meanwhile, the holes in the VB of g-CN are consumed by TEOA. Therefore, the presence of Ni-Mo alloys co-catalyst can effectively separate and transfer the photogenerated holes and electrons, which leads to remarkably enhance photocatalytic H<sub>2</sub> production performance of g-CN. In general, the greatly improved

photocatalytic H<sub>2</sub> production activity of Ni-Mo/g-C<sub>3</sub>N<sub>4</sub> is mainly attributed to the presence of Ni-Mo alloys, which not only enhances the light absorbance but also effectively promote the separation of photo-generated holes and electrons. Therefore, the new noble-metal-free Ni-Mo nanoparticles can be used instead of Pt as an active co-catalyst for drastically enhanced photocatalytic H<sub>2</sub> generation activity over g-C<sub>3</sub>N<sub>4</sub>. The amount of the Ni-Mo nanoparticles can be reduced by further reducing its particle size and increasing its uniformity of the distribution on g-C<sub>3</sub>N<sub>4</sub>. Optimization of the system to further improve the efficiency is ongoing in our lab.

#### 4. Conclusions

In conclusion, a new Ni-Mo/g-C<sub>3</sub>N<sub>4</sub> photocatalyst has been prepared by modifying Ni-Mo nanoparticles on the surface of g-C<sub>3</sub>N<sub>4</sub>, and the novel photocatalyst exhibits the efficient photocatalytic H<sub>2</sub> generation activity. The photocatalytic H<sub>2</sub> evolution rate of the Ni-Mo/g-C<sub>3</sub>N<sub>4</sub> photocatalysts (1785 μmol g<sup>-1</sup> h<sup>-1</sup>) is about 37 times higher than that of bare g-C<sub>3</sub>N<sub>4</sub> (48 μmol g<sup>-1</sup> h<sup>-1</sup>), which is even as high as the optimized Pt/g-C<sub>3</sub>N<sub>4</sub>, and the photocatalysts also has good stability for photocatalytic H<sub>2</sub> evolution. The present good performance of Ni-Mo/g-C<sub>3</sub>N<sub>4</sub> is mainly attributed to the presence of Ni-Mo alloys, which effectively promote the separation and suppress the recombination of photogenerated electrons and holes. Our findings represent that utilizing the noble-metal-free, low-cost elements and rich in nature Ni-Mo alloys as co-catalytic materials can be applied widely to harvest steady and cost-effective solar energy based on semiconductor photocatalysts.

#### Acknowledgements

We gratefully acknowledge the financial supports by NSF of China (No. 51572046, 61775131), MOE of China (No.111-2-04, IRT\_16R13), STC of Shanghai (16JC1400700, 15ZR1401200, 16XD1400100), SMEC

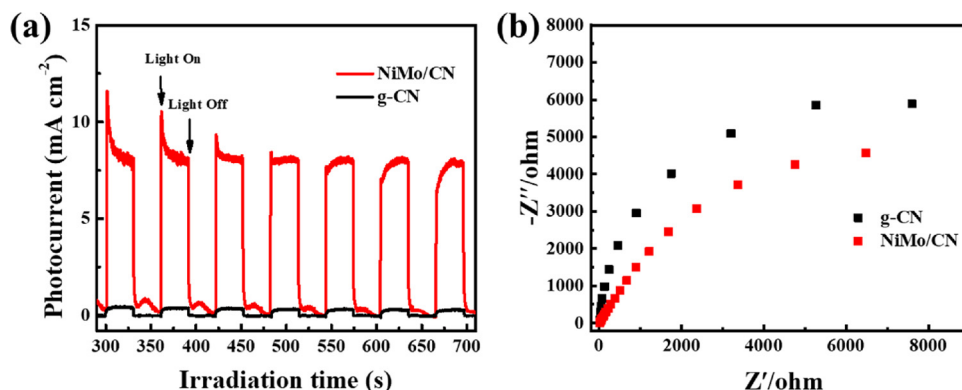


Fig. 8. Periodic on/off photocurrent response (a) and EIS Nyquist plots (b) of the g-CN and NiMo/CN samples.

(2017-01-07-00-03-E00055) and Eastern Scholar.

## Appendix A. Supplementary data

Supplementary material related to this article can be found, in the online version, at doi:<https://doi.org/10.1016/j.apcatb.2018.10.003>.

## References

- X. Zong, H. Yan, G. Wu, G. Ma, F. Wen, L. Wang, C. Li, Enhancement of photo-catalytic H<sub>2</sub> evolution on CdS by loading MoS<sub>2</sub> as cocatalyst under visible light irradiation, *J. Am. Chem. Soc.* 130 (2008) 7176–7177, <https://doi.org/10.1021/ja8007825>.
- W.-F. Chen, K. Sasaki, C. Ma, A.I. Frenkel, N. Marinkovic, J.T. Muckerman, Y. Zhu, R.R. Adzic, Hydrogen-evolution catalysts based on non-noble metal Nickel–Molybdenum nitride nanosheets, *Angew. Chem. Int. Ed.* 51 (2012) 6131–6135, <https://doi.org/10.1002/anie.201200699>.
- D. Xu, Y. Rui, V.T. Mbah, Y. Li, Q. Zhang, H. Wang, Binary nickel and iron oxide modified Ti-doped hematite photoanode for enhanced photoelectrochemical water splitting, *Int. J. Hydrog. Energy.* 41 (2016) 873–881, <https://doi.org/10.1016/j.ijhydene.2015.10.113>.
- J.J. Zhao, P.F. Liu, Y.L. Wang, Y.H. Li, M.Y. Zu, C.W. Wang, X.L. Wang, L.J. Fang, H.D. Zeng, H. Yang, Metallic Ni<sub>3</sub>P/Ni co-catalyst to boost photocatalytic hydrogen evolution, *Chem. Eur. J.* 23 (2017) 16734–16737, <https://doi.org/10.1002/chem.201704040>.
- M. Zhu, S. Kim, L. Mao, M. Fujitsuka, J. Zhang, X. Wang, T. Majima, Metal-free photocatalyst for H<sub>2</sub> evolution in visible to near-infrared region: black phosphorus/graphitic carbon nitride, *J. Am. Chem. Soc.* 139 (2017) 13234–13242, <https://doi.org/10.1021/jacs.7b08416>.
- Y. Hou, A.B. Laursen, J. Zhang, G. Zhang, Y. Zhu, X. Wang, S. Dahl, I. Chorkendorff, Layered nanojunctions for hydrogen-evolution catalysis, *Angew. Chem.* 125 (2013) 3709–3713, <https://doi.org/10.1002/ange.201210294>.
- Y. Zhu, Y. Xu, Y. Hou, Z. Ding, X. Wang, Cobalt sulfide modified graphitic carbon nitride semiconductor for solar hydrogen production, *Int. J. Hydrog. Energy.* 39 (2014) 11873–11879, <https://doi.org/10.1016/j.ijhydene.2014.06.025>.
- X. Wang, K. Maeda, A. Thomas, K. Takanabe, G. Xin, J.M. Carlsson, K. Domen, M. Antonietti, A metal-free polymeric photocatalyst for hydrogen production from water under visible light, *Nat. Mater.* 8 (2009) 76–80, <https://doi.org/10.1038/nmat2317>.
- J. Liu, Q. Jia, J. Long, X. Wang, Z. Gao, Q. Gu, Amorphous NiO as co-catalyst for enhanced visible-light-driven hydrogen generation over g-C<sub>3</sub>N<sub>4</sub> photocatalyst, *Appl. Catal. B Environ.* 222 (2018) 35–43, <https://doi.org/10.1016/j.apcatb.2017.09.073>.
- Y. Xu, M. Kraft, R. Xu, Metal-free carbonaceous electrocatalysts and photocatalysts for water splitting, *Chem. Soc. Rev.* 45 (2016) 3039–3052, <https://doi.org/10.1039/C5CS00729A>.
- S. Yang, Y. Gong, J. Zhang, L. Zhan, L. Ma, Z. Fang, R. Vajtai, X. Wang, P.M. Ajayan, Exfoliated graphitic carbon nitride nanosheets as efficient catalysts for hydrogen evolution under visible light, *Adv. Mater.* 25 (2013) 2452–2456, <https://doi.org/10.1002/adma.201204453>.
- X. Han, D. Xu, L. An, C. Hou, Y. Li, Q. Zhang, H. Wang, WO<sub>3</sub>/g-C<sub>3</sub>N<sub>4</sub> two-dimensional composites for visible-light driven photocatalytic hydrogen production, *Int. J. Hydrog. Energy.* 43 (2018) 4845–4855, <https://doi.org/10.1016/j.ijhydene.2018.01.117>.
- Z. Lin, X. Wang, Nanostructure engineering and doping of conjugated carbon nitride semiconductors for hydrogen photosynthesis, *Angew. Chem.* 125 (2013) 1779–1782, <https://doi.org/10.1002/ange.201209017>.
- C. Li, Y. Du, D. Wang, S. Yin, W. Tu, Z. Chen, M. Kraft, G. Chen, R. Xu, Unique P-Co-N surface bonding states constructed on g-C<sub>3</sub>N<sub>4</sub> nanosheets for drastically enhanced photocatalytic activity of H<sub>2</sub> evolution, *Adv. Funct. Mater.* 27 (2017) 1604328, <https://doi.org/10.1002/adfm.201604328>.
- J. Zhang, G. Zhang, X. Chen, S. Lin, L. Möhlmann, G. Dolega, G. Lipner, M. Antonietti, S. Blechert, X. Wang, Co-monomer control of carbon nitride semiconductors to optimize hydrogen evolution with visible light, *Angew. Chem. Int. Ed.* 51 (2012) 3183–3187, <https://doi.org/10.1002/anie.201106656>.
- Y. Hou, Y. Zhu, Y. Xu, X. Wang, Photocatalytic hydrogen production over carbon nitride loaded with WS < sru > 2 < /sub > as cocatalyst under visible light, *Appl. Catal. B Environ.* 156–157 (2014) 122–127, <https://doi.org/10.1016/j.apcatb.2014.03.002>.
- J.R. McKone, B.F. Sadtler, C.A. Werlang, N.S. Lewis, H.B. Gray, Ni–Mo nanopowders for efficient electrochemical hydrogen evolution, *ACS Catal.* 3 (2013) 166–169, <https://doi.org/10.1021/cs300691m>.
- J.R. McKone, E.L. Warren, M.J. Bierman, S.W. Boettcher, B.S. Brunschwig, N.S. Lewis, H.B. Gray, Evaluation of Pt, Ni, and Ni–Mo electrocatalysts for hydrogen evolution on crystalline Si electrodes, *Energy Environ. Sci.* 4 (2011) 3573–3583, <https://doi.org/10.1039/C1EE01488A>.
- J.M. Jakšić, M.V. Vojnović, N.V. Krstajić, Kinetic analysis of hydrogen evolution at Ni–Mo alloy electrodes, *Electrochim. Acta* 45 (2000) 4151–4158, [https://doi.org/10.1016/S0013-4686\(00\)00549-1](https://doi.org/10.1016/S0013-4686(00)00549-1).
- P. Prioteasa, F. Golgovici, G. Sbircea, L. Anicai, T. Visan, Electrodeposition, structure and corrosion behaviour of Ni–Mo alloys from citrate Aqueous electrolyte, *Rev. Chim.* 61 (2010) 1046–1053.
- E.J. Podlaha, D. Landolt, Induced codeposition I. An experimental investigation of Ni–Mo alloys, *J. Electrochim. Soc.* 143 (1996) 885–892, <https://doi.org/10.1149/1.1836553>.
- Y. Li, R. Jin, Y. Xing, J. Li, S. Song, X. Liu, M. Li, R. Jin, Macroscopic foam-like holey ultrathin g-C<sub>3</sub>N<sub>4</sub> nanosheets for drastic improvement of visible-light photocatalytic activity, *Adv. Energy Mater.* 6 (2016) 1601273, <https://doi.org/10.1002/aenm.201601273>.
- W. Ni, B. Wang, J. Cheng, X. Li, Q. Guan, G. Gu, L. Huang, Hierarchical foam of exposed ultrathin nickel nanosheets supported on chainlike Ni-nanowires and the derivative chalcogenide for enhanced pseudocapacitance, *Nanoscale* 6 (2014) 2618–2623, <https://doi.org/10.1039/C3NR06031D>.
- M. Quan Yu, Y. Hang Li, S. Yang, P. Fei Liu, L. Feng Pan, L. Zhang, H. Gui Yang, Mn<sub>3</sub>O<sub>4</sub> nano-octahedrons on Ni foam as an efficient three-dimensional oxygen evolution electrocatalyst, *J. Mater. Chem. A* 3 (2015) 14101–14104, <https://doi.org/10.1039/C5TA02988K>.
- J.G. Highfield, E. Claude, K. Oguro, Electrocatalytic synergism in Ni/Mo cathodes for hydrogen evolution in acid medium: a new model, *Electrochim. Acta* 44 (1999) 2805–2814, [https://doi.org/10.1016/S0013-4686\(98\)00403-4](https://doi.org/10.1016/S0013-4686(98)00403-4).
- W. Sen-Lin, Z. Yi, Preparation and electrocatalytic performance of Ni-Mo/LaNi<sub>5</sub> porous composite electrode toward hydrogen evolution reaction, *Acta Phys. Chim. Sin.* 27 (2011) 1417–1423, <https://doi.org/10.3866/PKU.WHB20110510>.
- X. Wang, S. Blechert, M. Antonietti, Polymeric graphitic carbon nitride for heterogeneous photocatalysis, *ACS Catal.* 2 (2012) 1596–1606, <https://doi.org/10.1021/cs300240x>.
- S. Ye, R. Wang, M.-Z. Wu, Y.-P. Yuan, A review on g-C<sub>3</sub>N<sub>4</sub> for photocatalytic water splitting and CO<sub>2</sub> reduction, *Appl. Surf. Sci.* 358 (Part A) (2015) 15–27, <https://doi.org/10.1016/j.apsusc.2015.08.173>.
- W.-J. Ong, L.-L. Tan, Y.-H. Ng, S.-T. Yong, S.-P. Chai, Graphitic carbon nitride (g-C<sub>3</sub>N<sub>4</sub>)-based photocatalysts for artificial photosynthesis and environmental remediation: are We A step closer to achieving sustainability? *Chem. Rev.* 116 (2016) 7159–7329, <https://doi.org/10.1021/acs.chemrev.6b00075>.
- H. Kasap, C.A. Caputo, B.C.M. Martindale, R. Godin, V.W. Lau, B.V. Lotsch, J.R. Durrant, E. Reisner, Solar-driven reduction of aqueous protons coupled to selective alcohol oxidation with a carbon nitride–molecular Ni catalyst system, *J. Am. Chem. Soc.* 138 (2016) 9183–9192, <https://doi.org/10.1021/jacs.6b04325>.
- S.-S. Yi, J.-M. Yan, B.-R. Wu, S.-J. Li, K.-H. Liu, Q. Jiang, Noble-metal-free cobalt phosphide modified carbon nitride: an efficient photocatalyst for hydrogen generation, *Appl. Catal. B Environ.* 200 (2017) 477–483, <https://doi.org/10.1016/j.apcatb.2016.07.046>.
- O. Fontelles-Carceler, M.J. Muñoz-Batista, M. Fernández-García, A. Kubacka, Interface effects in sunlight-driven Ag/g-C<sub>3</sub>N<sub>4</sub> composite catalysts: study of the toluene photodegradation quantum efficiency, *ACS Appl. Mater. Interfaces* 8 (2016) 2617–2627, <https://doi.org/10.1021/acsami.5b10434>.
- K. Fan, Z. Jin, H. Yang, D. Liu, H. Hu, Y. Bi, Promotion of the excited electron transfer over Ni- and Co-sulfide co-doped g-C<sub>3</sub>N<sub>4</sub> photocatalyst (g-C<sub>3</sub>N<sub>4</sub>/Ni<sub>1-x</sub>Co<sub>x</sub>S<sub>2</sub>) for hydrogen production under visible light irradiation, *Sci. Rep.* 7 (2017) 7710, <https://doi.org/10.1038/s41598-017-08163-y>.
- L.S. Sanches, S.H. Domingues, C.E.B. Marinho, L.H. Mascaro, Characterisation of electrochemically deposited Ni–Mo alloy coatings, *Electrochim. Commun.* 6 (2004) 543–548, <https://doi.org/10.1016/j.elecom.2004.04.002>.
- Q. Yao, Z.-H. Lu, W. Huang, X. Chen, J. Zhu, High Pt-like activity of the Ni–Mo/graphene catalyst for hydrogen evolution from hydrolysis of ammonia borane, *J. Mater. Chem. A* 4 (2016) 8579–8583, <https://doi.org/10.1039/C6TA002004F>.
- Z. Sun, H. Zheng, J. Li, P. Du, Extraordinarily efficient photocatalytic hydrogen evolution in water using semiconductor nanorods integrated with crystalline Ni<sub>2</sub>P cocatalysts, *Energy Environ. Sci.* 8 (2015) 2668–2676, <https://doi.org/10.1039/C5EE01310K>.
- Q. Han, B. Wang, J. Gao, Z. Cheng, Y. Zhao, Z. Zhang, L. Qu, Atomically thin mesoporous nanomesh of graphitic C<sub>3</sub>N<sub>4</sub> for high-efficiency photocatalytic hydrogen evolution, *ACS Nano.* 10 (2016) 2745–2751, <https://doi.org/10.1021/acsnano.5b07831>.
- G. Zhang, Z.-A. Lan, L. Lin, S. Lin, X. Wang, Overall water splitting by Pt/g-C<sub>3</sub>N<sub>4</sub> photocatalysts without using sacrificial agents, *Chem. Sci.* 7 (2016) 3062–3066, <https://doi.org/10.1039/C5SC04572J>.
- X. An, W. Wang, J. Wang, H. Duan, J. Shi, X. Yu, The synergistic effects of Ti<sub>3</sub>C<sub>2</sub> MXene and Pt as co-catalysts for highly efficient photocatalytic hydrogen evolution over g-C<sub>3</sub>N<sub>4</sub>, *Phys. Chem. Chem. Phys.* 20 (2018) 11405–11411, <https://doi.org/10.1039/C8CP01123K>.
- L. Bi, X. Gao, L. Zhang, D. Wang, X. Zou, T. Xie, The enhanced photocatalytic hydrogen evolution of NiCoP/g-C<sub>3</sub>N<sub>4</sub> with the improved separation efficiency and charge transfer efficiency, *ChemSusChem.* 11 (2018) 276–284, <https://doi.org/10.1002/cssc.201701574>.
- Y. Zhao, Y. Wang, X. Liu, J. Liu, B. Han, X. Hu, F. Yang, Z. Xu, Y. Li, S. Jia, Z. Li, Carbon quantum dot implanted graphite carbon nitride nanotubes: excellent charge separation and enhanced photocatalytic hydrogen evolution, *Angew. Chem. Int. Ed.* 57 (2018) 5765–57714, <https://doi.org/10.1002/anie.201802014>.
- W. Tu, Y. Zhou, Q. Liu, S. Yan, S. Bao, X. Wang, M. Xiao, Z. Zou, An in situ simultaneous reduction-hydrolysis technique for fabrication of TiO<sub>2</sub>-graphene 2D sandwich-like hybrid nanosheets: graphene-promoted selectivity of photocatalytic-driven hydrogenation and coupling of CO<sub>2</sub> into methane and ethane, *Adv. Funct. Mater.* 23 (2013) 1743–1749, <https://doi.org/10.1002/adfm.201202349>.
- H. Yu, R. Shi, Y. Zhao, T. Bian, Y. Zhao, C. Zhou, G.I.N. Waterhouse, L.-Z. Wu, C.-H. Tung, T. Zhang, Alkali-assisted synthesis of nitrogen deficient graphitic carbon nitride with tunable band structures for efficient visible-light-driven hydrogen evolution, *Adv. Mater.* (2017) 1615048–1615055, <https://doi.org/10.1002/adma.201605148>.
- M. Shao, Y. Shao, J. Chai, Y. Qu, M. Yang, Z. Wang, M. Yang, W.F. Ip, C.T. Kwok, X. Shi, Z. Lu, S. Wang, X. Wang, H. Pan, Synergistic effect of 2D Ti<sub>2</sub>C and g-C<sub>3</sub>N<sub>4</sub> for efficient photocatalytic hydrogen production, *J. Mater. Chem. A* 5 (2017) 16748–16756, <https://doi.org/10.1039/C7TA04122E>.